Controlling the Electrical Properties of Reactively Sputtered High Entropy Alloy CrFeNiCoCu Films

J. Mayandi[1,2] · T. G. Finstad[1,4] · M. Stange[3] · G. C. Vásque[1] · M. F. Sunding[3] · O. M. Løvvik[1,4] · S. Diplas[3,5] · P. A. Carvalho[3,6]

Abstract

Oxide-containing films were made by reactively sputtering a high-entropy alloy target of CrFeCoNiCu. We report on a wide range of changes to the electrical properties made by different heat treatments in oxidizing and reducing atmospheres, respectively. We combine temperature-dependent Hall effect measurements down to 10 K to study the transport mechanisms and correlate that with structural measurements by x-ray diffraction and scanning electron microscopy. The measured/effective resistivity could be varied between 1.3×10^{-4} Ω cm and 1.2×10^{-3} Ω cm by post-deposition processing. The temperature coefficient of resistivity could be varied between -1.2×10^{-3} K^{-1} through 0 and to $+0.7 \times 10^{-3}$ K^{-1}. The key to the variation is controlling the morphology and topology of the film. The conduction of charge carriers is dominated by the relative contribution of weak localization and alloy scattering by varying the degree of disorder in the metallic high-entropy alloy and its topology.

Keywords High-entropy alloy · thin film current transport · sputtering

Introduction

There has been an increasing interest in material science towards high-entropy alloys (HEA)[1–4] that has been followed by a very large interest in high-entropy oxides (HEO).[5–10] The main applications of HEA have been as construction materials with specific properties.[11,12] There has also been an increased interest in the oxidation of HEAs,[13] which is motivated by the structural materials for varying environments. While most work on both HEAs and HEOs have been on bulk material, there has also been an increasing interest for making these materials as thin films.[14,15] Hard coatings and corrosion-resistant coatings are important applications. Interest in HEAs and HEOs for various other industrial and technological applications have also appeared.[6,16,17] Among interesting examples of HEO applications are that they have shown high activity in several catalytic reactions under different processes such as thermo-, electro-, and photo-catalysis and have good performance for CO oxidation, alcohol oxidation, CH_4 partial oxidation, CO_2 hydrogenation, desulfurization with oxidation, water oxidation and water splitting.[18] HEOs have also been applied as anode material in Li-ion batteries for high-capacity storage of electrochemical energy,[19,20] and used as protective coatings for mechanical parts, such as cutting tools and drills, which usually work under high-temperature corrosive environments.[21] Further, HEO films with colossal dielectric constants have been reported[22] and suggested for future generations of thin film transistors.

HEAs are typically made up of five elements or more in near equal atomic concentration proportions.[23] Many HEAs are reported to show simple single-phase or dual-phase solid solution phases, without the formation of intermetallic compounds that are observed for many traditional metal alloy

✉ T. G. Finstad
terje.finstad@fys.uio.no

1 Centre for Materials Science and Nanotechnology, University of Oslo, Oslo, Norway

2 Department of Materials Science, School of Chemistry, Madurai Kamaraj University, Madurai, India

3 Department of Sustainable Energy Technology, SINTEF Industry, Oslo, Norway

4 Department of Physics, University of Oslo, Oslo, Norway

5 Department of Chemistry, University of Oslo, Oslo, Norway

6 CEFEMA, Instituto Superior Tecnico, Technical University of Lisbon, Lisbon, Portugal

systems.[24] The entropy of such mixtures has been considered a possibility to stabilize the alloys in those simple solid solution phases.[1] The simple phases are face-centered cubic (FCC) or cubic-centered cubic (BCC). Sometimes, systems tested for HEA behavior show more complicated secondary phases, which may be a reason for naming these systems complex concentrated alloys (CCA) or other names.[25,26] HEOs are similarly oxides where there are five or more cation elements, but a single-phase crystal structure is often assumed and with no ordering among the cations.[27]

It has been widely cited that many of the reported physical and mechanical properties of HEAs are due to local lattice strain caused by the atoms being displaced away from the ideal lattice site.[28] Simulations have created that situation with suitable interatomic potentials[29] and efforts to measure the local strain by diffuse scattering techniques have been reported.[30] The excellent hardness of some HEAs have been linked to this distortion.[31] The lattice distortion also influences the electrical conductivity of the materials.

The material reported in the present work is made by reactive sputtering from an HEA target made up of equal amounts of five 3d-transition metals, CrFeCoNiCu, and then given heat treatments. This HEA has been reported on in the literature.[1,12,25,29,32–44] The crystal structure has been reported to be FCC, either as a solid solution phase with uniform composition, or as two solid solution phases with slightly different compositions. We have observed that sputtered CrFeCoNiCu has a single FCC phase.[44] With the addition of oxygen, either during deposition or by annealing in oxygen, Cr is preferentially oxidized, which alters the stability of the remaining alloy, which then decomposes into two different FCC structures, and for extended annealing time, also into a BCC structure.[44]

In this work, we report on the electrical properties of reactively sputtered CrFeCoNiCu in oxygen-containing plasma, resulting in a composite film. We report on tuning properties of the composite material by varying the morphology. The building blocks in the composite are essentially HEAs and HEOs. Sputtering is a nonequilibrium process, here producing a metastable film. The deposited films contain oxygen and they decompose under annealing yielding a change in the electrical properties. For each annealing we report on the electrical properties and the structural change. We will present the temperature dependence of the (effective) resistivity down to 10 K. This may have direct practical applications as well as a fundamental significance. For a single film deposition the resistivity and its temperature coefficient can be systematically varied over a wide range by different heat treatments.

Experimental

The films were deposited on quartz or silica wafer substrates by magnetron sputtering from a custom-made sputtering target (HR Anlagenbau, GmbH) consisting of equal amounts of Fe, Cr, Co, Ni and Cu. During the sputtering, the working gas ambience was argon:oxygen with a flow ratio of 92:8 and total working gas pressure about 0.4 Pa. A DC power of 200 W was applied. No intentional substrate heating was used during the sputtering, and the substrates were rotated during deposition to obtain lateral uniformity. The composition of the films was characterized by EDS.

The films on substrates were cleaved into small sample pieces (~ 1 cm × 1 cm square) and characterized by structure evaluations and transport measurements. Some sample pieces were also annealed in a furnace in flowing oxygen (purity 99.999%) or in a nitrogen:hydrogen (90:10) mixture (NHM) ambience.

The areal density of the films was measured by Rutherford backscattering spectrometry. The films were characterized by x-ray diffraction (XRD) characterization using normal θ–2θ scans (locked-couple mode) to determine the preferred crystal orientation and changes in phase with annealing). The surface morphology of the films was analyzed by scanning electron microscopy (not shown). The transport characterization consisted of electrical DC Hall and van der Pauw measurements (Lake Shore, 7704 HMS) to observe the temperature dependence of the resistivity.

Hypothesis

We start by presenting a hypothesis for the system we have measured at various stages of the film treatment, although with a somewhat wider applicability than for the observations reported here. It basically consists of considering the films to consist of separate regions as sketched in Fig. 1. There are regions or nanograins of different metallic HEA with different compositions of the metals Cr, Fe, Co, Ni and Cu and also with different metastable concentrations of oxygen. Further, there are regions or nanograins of different oxides, with different stoichiometry. The oxides are derived from the oxides of the metals. The electrical properties of the film as a whole will be that of an effective medium where the electrical properties of the different parts can be quite different. The electrical properties of the films come mainly from conduction through the most conducting parts, such as percolation through the HEA metallic parts. The hypothesis predicts that the electrical properties of the film can be controlled by varying the

Fig. 1 Artistic schematics of (the top) the topography of the films prepared by reactive sputtering with nanograins of HEA connected by oxide grains. The bottom shows the corresponding lateral energy state diagram. Transport of carriers in the structure is also indicated. The topography can be varied by annealing in reducing or oxidizing ambient.
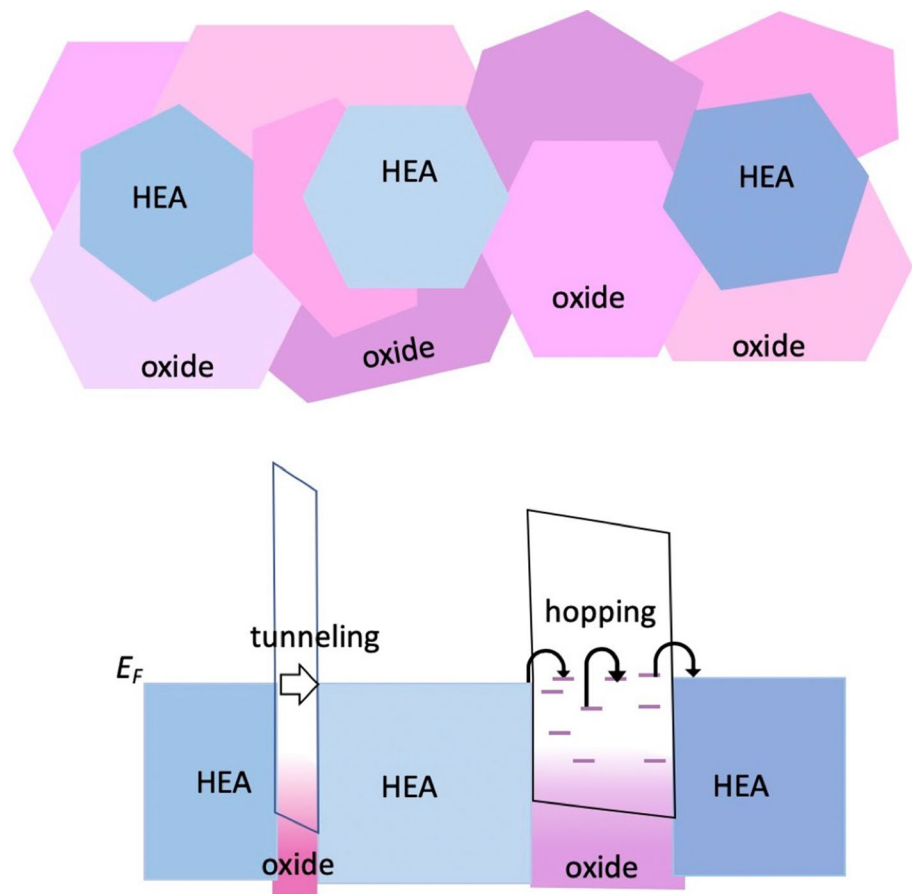
fraction of oxide to metallic HEA and their topology and this can be varied by controlled annealing in oxidizing atmosphere and reducing atmosphere for a given sputtering. The hypothesis also implies that this ratio can be varied by varying the sputtering conditions, but that effect will not be addressed in this report.

The electrical transport in the HEA will then be different by the different topologies. This change can be measured by simply measuring the resistance giving the effective resistivity of the film. Measurement as a function of temperature will give some more information of which process in which part of the system is limiting the transport. Transport in an HEA will have a resistance higher than that of pure metals due to the disorder in the potential created by the arrangement of different d-metal atoms in a non-ordered sequence, which also creates local lattice distortions. This alloy scattering is temperature-independent. The phonon scattering will typically have a contribution to the resistivity being proportional to T when going to the higher temperature regime. The disorder in an HEA may increase by uptake of oxygen. Then the electron wavefunction may experience weak localization resulting in a characteristic temperature dependence. The current through the film may be through communication between HEA grains directly or by tunneling. Tunneling has

no temperature dependence, so it cannot be discriminated from alloy scattering or grain boundary scattering. The current could go through part of oxides by variable range hopping, as described by Mott theory[45] or the Efros–Shklovskii theory.[46] Stallinga[47] has stated that "there are nearly as many models as there are publications in the literature or measurement sets" on variable range hopping/percolation.

Results and Discussion

Electrical Characterization

Resistivity versus Temperature of As-Deposited (ASD) Films

The resistivity, ρ, of the as-deposited (ASD) film sample was measured to be 857 μΩ cm at room temperature (RT). Figure 2a shows resistivity measured from low temperature up to RT. The dominating conductivity type was p-type for the whole temperature range as indicated by the sign of the Hall voltage measured simultaneously.

The resistivity at RT (860 μΩ cm) is high compared to Cu (1.6 μΩ cm) and also high compared to the CrFeCoNiCu-HEA (140 μΩ cm).[44] It is seen from Fig. 2b that the
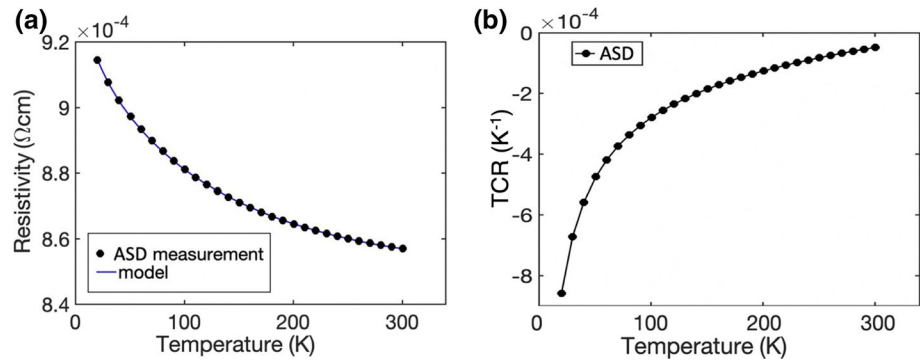
temperature coefficient of resistivity, $TCR = \partial\ln(\rho)/\partial T$, is always negative, with a relatively small absolute value. So, the absolute value of the resistivity is higher than that of the Mott–Ioffe–Regel limit for metallic conductance ($\approx 100\ \mu\Omega$ cm),[44] and given the negative TCR, the conductance in the film is not metallic. We can model the temperature dependence of the resistivity very well as seen from the solid line in Fig. 2a. However, when the variations are small and the data and model vary smoothly, one should be syllogistic about the significance of the excellent match. We get an excellent match of the curve by an expression containing temperature-independent alloy scattering and weak localization. We will use other terms for other samples and fit all data by the following expression.

$$\rho(T) = r_0 + r_{wl}\sqrt{T} + r_{BG}T + r_{ee}T^2 \quad (1)$$

Here r_0 contains resistance due to temperature-independent alloy scattering and the constant associated with weak localization. The negative coefficient r_{wl} gives the quantum mechanical correction for weak localization,[44] and dominates the temperature dependence in Fig. 2. The other terms are included in order to use the same expression for the annealed samples. Here r_{BG} describes the phonon-electron scattering interaction which dominates for pure metals where it is constant at higher temperatures given that the resistivity then increases linearly with temperature or else varies as the Bloch-Grüneisen relation.[44] The parameter r_{ee} describes electron-electron interactions. It is the weak localization term that gives the negative slope of the resistivity curve. A negative slope could in principle also be due to variable range hopping (VRH), it would have had a contribution to the resistivity going as

$$\rho_{VRH}(T) = r_{VRH}e^{(\Delta E/kT)^\beta} \quad (2)$$

with $\beta = 0.25$ for the famous Mott theory[45] and $\beta = 0.5$ for the Efros–Shklovskii theory,[46] while experiments on polymers have reported β from 2 and downwards.[47] However, in the current case, the VRH expression does not fit with the experimental data, so we do not include it in our

analysis. However, for the case of exchanging Cr with Ge and increasing the oxygen flow ratio for reactively sputtered FeCoNiCuGe, it fits well.[48] Another effect which can give a negative slope of the resistivity is the Kondo effect giving a term ρ_K[49,50]

$$\rho_K(T) = r_K\ln\left(\frac{\mu}{T}\right) \quad (3)$$

where r_K is here a fitting parameter characterizing the strength which is proportional to the exchange integral between interacting spins. The effect of μ, which is a characteristic temperature, is to shift the baseline. This effect is observed for materials with magnetic impurities and only dominates at the lowest temperatures and not all the way up to RT. For homogenous CrFeCoNiCu films we have observed that the Kondo effect cannot be distinguished from weak localization by the temperature dependence of the resistivity.[44] Therefore, we cancel that parameter in the fitting model of the system here.

We interpret the data of Fig.2a as that the resistive part of the transport is dominated by regions in the film which are essentially creating a connected network, but where the parts consisting of HEA nanocrystals are very damaged with respect to the periodicity of the lattice. The weak localization arises from the heavily distorted lattice. We argue that the lattice is more distorted than what is caused by randomization of the sequence order of the-metal elements. The argument for that is that for sputtered HEA CrFeCoNiCu films the resistivity has a negative TCR only at the very lowest temperature.[44] The present dominance of weak disorder may arise from (metastable) solution of oxygen atoms in the HEA grains.

The electrical measurement data is challenging to analyze further on a material level, and even more so quantitatively in terms of local disorder, when the properties are nonuniform. However, the variation of the resistivity can be understood qualitatively. We have also measured the Hall coefficient R_H and from that and the resistivity calculated the Hall mobility as shown in Fig. 3. These parameters are by themselves controversial and complicated to interpret for

homogenous distorted/defective materials and beyond the scope of the current paper to treat for an inhomogeneous film. Here we just comment that the temperature coefficient of R_H is positive while for distorted films of NbN reported by Chand et al.[51] it is negative and the ratio between the temperature coefficient for ρ and R_H is a constant in that case, which is quite different than what is observed here.

Here we remark that the sign of the Hall voltage indicates that the sample is p-type over the whole temperature range 20–300 K. We also measured the Seebeck coefficient of the sample from RT and upwards, and the polarity of the Seebeck voltage indicates that the sample is n-type. These are the same polarities for the Hall coefficient and the Seebeck coefficient as what we have observed for films of CrFeCoNiCu.[44] Those observations indicate that CrFeCoNiCu-HEA has both electrons and holes at the Fermi level. Then R_H and the Seebeck coefficient both have contributions from holes as well as electrons, but the weight factors in the expressions are different for the two coefficients. Thus, the present observations are in agreement with the idea that it is the HEA nanograins in the film that give the dominating carriers transported in it.

Resistivity versus Temperature after Annealing in NMH

The resistivity of the samples was measured after annealing in the reducing atmosphere of forming gas (nitrogen–hydrogen mixture, NHM). The results are shown in Fig. 4.

It is seen in Fig. 4a that the resistivity is changed much by the annealing and is reduced by each annealing step up to 500°C. Each of the curves also varies little with the measurement temperature and the curves appear almost flat when plotted in a linear scale including all the annealing temperatures as in Fig. 4a. In order to visually examine the temperature dependence of each curve, we display in Fig. 4b the resistivity minus the minimum taken from Fig. 4a. Also, in Fig. 4c is seen the TCR for each curve.

It is seen that the TCR is negative for all temperatures in the ASD case. After each annealing at successively higher temperature the TCR increased. It changes from all negative for the ASD case, through negative at low measurement temperatures and positive at high measurement temperatures for the 300°C and 400°C annealing, to being positive for essentially the whole measurement temperature range for the 500°C annealing case.

Fig. 3 Temperature-dependent Hall measurement results on films prepared by reactive sputtering of target made by CrFeCoNiCu with a flow rate ratio of Ar to O_2 of 92:8. (a) The Hall coefficient (b) The Hall mobility.
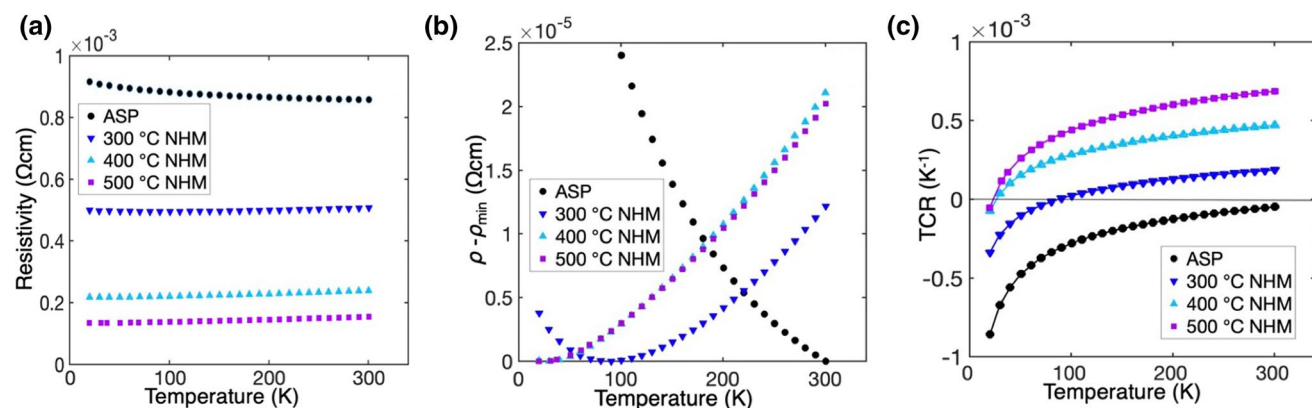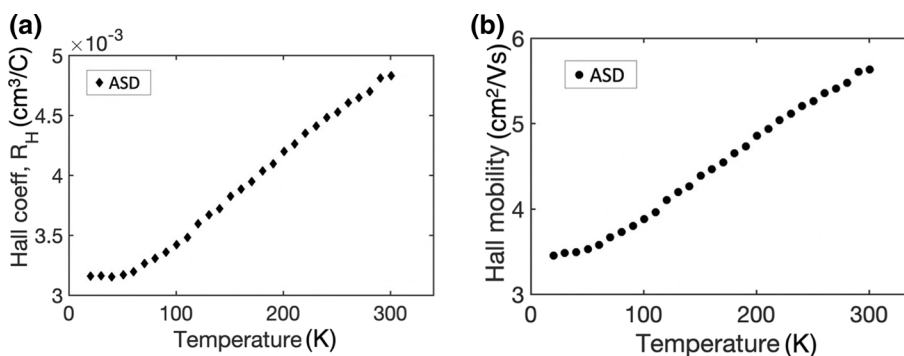

Fig. 4 Temperature dependence of the resistivity of the films prepared by reactive sputtering after annealing in nitrogen hydrogen mixture (NHM) for 2 h at the temperatures indicated. ASD is the as deposited film. (a) The resistivity. (b) The minimum of each curve subtracted from its resistivity. (c) The temperature coefficient of resistivity; TCR $= 1/\rho \cdot \partial\rho/\partial T$.

All the curves of Fig. 4a can be fitted very well with the expression of Eq. 1. The values of the fitting are shown in Table I. It is seen from that table that r_0 and r_{wl} are the parameters that vary the most, and there the resistance of the film decreases and weak-localization becomes less dominating. These observed features are consistent with the following hypothetic changes in the film: annealing alone causes atomic mobility change and rearrangements of the atoms in the film. The weak localization was caused by disorder in the metal-rich regions; we argued it was enhanced by oxygen atoms in the ASD case. If that segregates out of the HEA region, the weak localization character of the resistivity will diminish. For low anneal temperature, the oxygen may segregate as metal oxide, whereas for higher NHM annealing temperatures the oxide will be reduced. The metal oxide that has the highest tendency to form is that of Cr. The HEA region will then experience less Cr giving it less stability and it will have a tendency to form regions with less complexity by forming regions richer in Co-Fe and Cu-Ni. This will cause higher order and less weak localization contribution and also less alloy scattering contribution. The heat treatment and segregation are also most likely accompanied by grain growth and annealing out structural defects yielding less scattering and lower resistivity of regions. However,

since the film is nonuniform, we cannot directly use the reduction in the measured resistivity to reflect the exact reduction in the HEA resistivity, since the parts of the system that contribute is probably not constant.

Resistivity versus Temperature after Annealing in O_2

The resistivity of the samples after annealing in O_2 is shown in Fig. 5, with the expanded scale in Fig. 5b and the TCR in Fig. 5c. As for NHM annealing (Fig.4), the measured resistivity curves changed much for different annealing temperature. A large reduction in the resistivity and reduction in the dominance of weak localization is seen for 300°C annealing compared to the ASD case, qualitatively similar to the case for NHM gas. However, the reduction of the resistivity is slightly less, and the reduction of the weak localization fingerprints are also slightly less than for the NHM case. We take this as an indication that the anneal temperature causes atomic mobility and the oxygen segregates out of the HEA grains giving less disorder, also involving Cr in the oxide causing some partial element separation of the different metals, as for the NHM case. However, with oxygen present in the annealing ambient, the oxides that are formed are not reduced. After annealing at 400°C in O_2 the resistivity has

Table I Parameters used for fitting the temperature dependence of resistivity to the expression in Eq. 1 in the text.

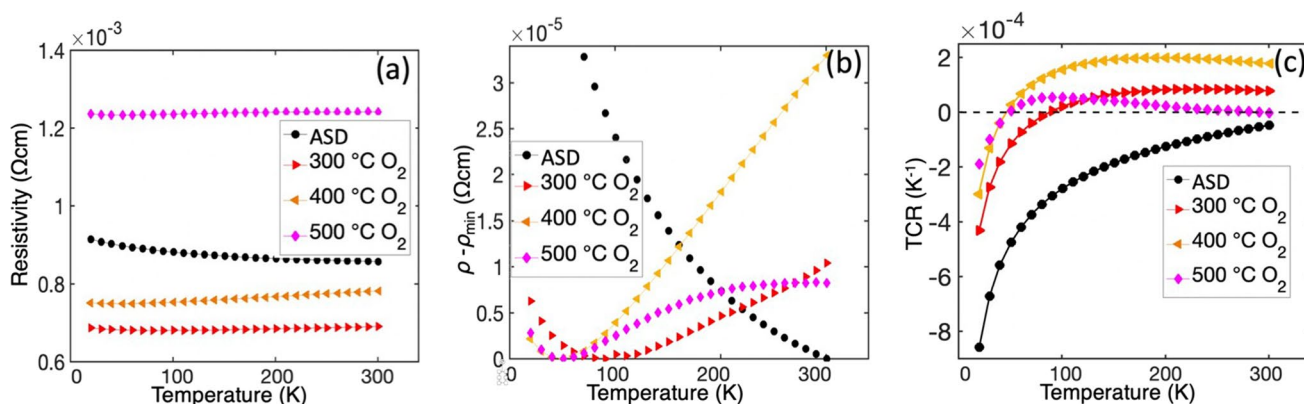| Sample\coeff.	r_0 (10^{-4} Ω)	r_{wl} (10^{-6} Ω $K^{-1/2}$)	r_{BG} (10^{-7} Ω K^{-1})	r_{ee} (10^{-11} Ω K^{-2})
ASD	9.49	-8.53	1.63	7.25
300°C NHM	5.08	-2.74	1.35	6.9
400°C NHM	2.8	-1.1	1.00	6.6
500°C NHM	1.3	-0.9	0.93	6.5
300°C O_2	7.05	-5.56	3.3	-19.3
400°C O_2	7.69	-6.15	4.7	-26.0
500°C O_2	12.46	-4.2	3.56	-44.0

Fig. 5 Temperature dependence of the resistivity of the films prepared by reactive sputtering after annealing in oxygen gas for 2 h at the temperatures indicated. ASD is the as-deposited film. (a) The resistivity (b) The minimum of each curve subtracted from its resistivity. (c) The temperature coefficient of resistivity; TCR = $1/\rho \cdot \partial\rho/\partial T$.

increased compared to the 300°C case. This increase we interpret as due to oxides forming in the film. One possibility is that it may create a network with reduced connectivity. For 500°C annealing the measured resistivity has increased much. The shape of the resist curve for that case is also different than those of the 300°C and 400°C; for increasing temperature, the value seems to go to saturation, or at least the slope is bending over and decreases. It is relevant to mention that there has been much works on resistivity saturation, both theoretically and experimentally.[52–56] Some theories predict a saturation for resistivities far below that in Fig. 5a, some metal systems have shown to follow that, while several reports of exceedance of the suggested limits have occurred. Some recent theories explain bending over of the resistivity curves as an indication that other transport channels become available at high temperatures, giving a change in the slope.[53] One should note that the fitting parameter r_{ee} in Table I for the O₂ annealing case is not physically sound. It is negative in that case and then has the effect of decreasing the slope at high temperatures, which provides a fitting.

Structure Characterization by XRD and SEM

Structure Evolution for Different Anneal Temperature, NHM Cases

Figure 6 shows SEM images of the surface of the film after annealing in forming gas for 2 h. Figure 6a is the ASD case. There is some contrast that evolves with annealing temperature into larger islands, from 10 nm to 50 nm diameter after 300°C (Fig. 6b) annealing to several µm after 500°C. (Fig. 6d). These islands appear to be Cu-rich on the surface as observed by EDX analysis. One example is shown in Fig. 7b for the case of 400°C annealing in NHM. This clearly shows that the film is nonuniform, caused by segregation of the metals and reflects a high surface mobility of Cu. The nonuniformity of the ASD film on the nanoscale cannot be seen from Fig. 6a, but can be seen qualitatively from the TEM analysis (not shown), from which it is also concluded that the film is nanocrystalline. From elemental scans it has been concluded that the elements are not distributed perfectly uniformly in the film: regions of the order of the nanocrystals had enhancement or reduction of the concentration of some elements. There are correlations between the region with enrichment for the different elements. Cr and oxygen are correlated, Co-Fe are correlated and Cu-Ni are correlated. We interpret that as a segregation. We rationalize that the segregations are partial, similar to spinodal decompositions, where there are concentration differences between different regions but not necessarily total depletion nor purification of an element in a region. This process with reactively sputtered CrFeCoNiCo may be phenomenologically similar to our observations for the oxygen interaction with HEA CrFeCoNiCo films,[44] where we observe that Cr is preferentially oxidized. This promotes concentration segregation of the other elements, also causing the appearance of FCC phases with different concentration and BCC phases. In the reactive sputtering case considered here, the atomic mobility during deposition is apparently large enough that we get some of these segregation phenomena.
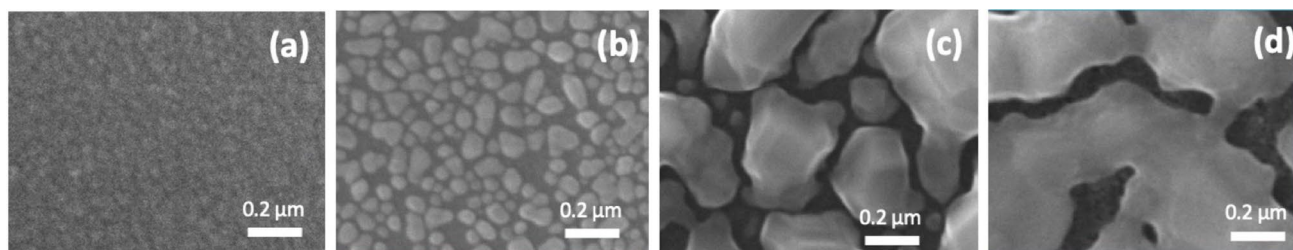

Fig. 6 SEM images of the sputtered films as deposited and annealed at different temperatures in NHM for 2 h. (a) As deposited (b) 300°C (c) 400°C (d) 500°C.

Fig. 7 EDX scan of the surface of a film annealed at 400°C in NHM for 2 h. (a) The SEM image indicating the scan path. (b) The EDX line scan. The blue dots are the Cu signals showing Cu-rich islands centered around the positions marked as 30 and 70 pixels.
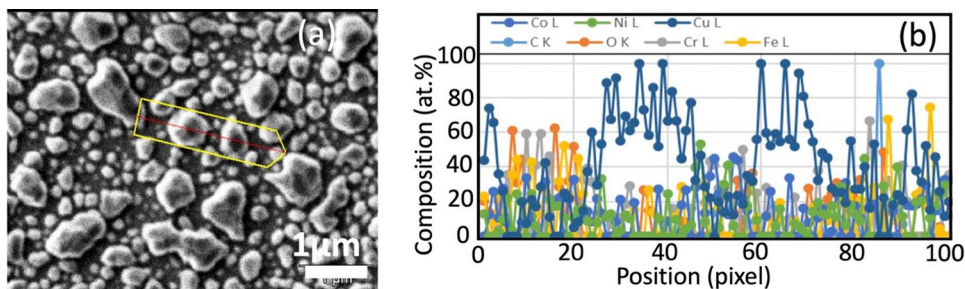
We have further information about the structure of the ASD case and the changes caused by annealing from our XRD data as shown in Fig. 8. The diffractogram curve of the ASD case shown in Fig. 8a has few features. The most pronounced is a broad peak around 43 degrees. From the HRTEM analysis the film is nanocrystalline, which we here consider to be distinct from amorphous. The film has texture, so we do not see contribution from all crystal planes of the nanocrystals. The large width of the peak for the ASD diffractogram arises from (1) small size of the nanocrystals, causing broadening ("Scherrer broadening"), (2) distortion of lattice due to different elements in the HEA, (3) contribution from different concentrations given the segregation seen in Fig. 8b. (4) Contribution from different crystal structures, both FCC and BCC, possibly HEO with NiO (Fm$\bar{3}$m, B1, #225) crystal structure. (5) HEA super-saturated with oxygen (6) Stress caused by formation of Cr_2O_3 on the grain boundaries.

It is seen from Fig. 8a that the XRD peaks become more distinct after annealing. The peak around 43° becomes stronger and sharper. It is connected to the (111) reflection of FCC. Also, the (200) from FCC is seen after annealing at 400°C and after 500°C. This is linked to the large segregation of Cu-rich islands seen in Figs. 6 and 7 and also linked to grain growth in the film. The diffractogram for 500°C in Fig. 9 also has a peak around 35° which can arise from an oxide. That would be an oxide that is not reduced by H_2 at 500°C. The peak position matches a spinel-type structure incorporating Cr, structurally like $FeCr_2O_3$.

Structure Evolution for Different Anneal Temperatures, O_2 Cases

Figure 9 shows SEM pictures of the surface of the films after being annealed in an oxygen ambient at different temperatures for 2 h. There is no contrast seen on the surface after 300°C annealing. There is also no significant change to the XRD diffractogram as can be seen in Fig. 8b. So, apparently the reactions in the film cause minor unobservable changes to the surface topology. From before, we know that CrFeCoNiCu HEA films react with O_2 to form a dense Cr oxide on the surface.[44] That may have happened here too. After 400°C, the SEM shows some contrast and a few white spots. After 500°C, seen in Fig. 9d, the contrast is more pronounced and the white spots have evolved into rod-like nanostructures, probably oxide nanorods. The formation of

Fig. 8 X-ray diffractograms using Cu Ka taken at RT. The y-axis has been offset for each diffraction curve. The vertical lines at the bottom are diffraction patterns for the crystal structures indicated which are relevant for the interpretation. FCC(Cu), BCC(Fe), NiO(Fm$\bar{3}$m), Cr_2O_3,$FeCr_2O_4$(I4$_1$/amd). (a) Samples annealed in NHM at different temperatures as indicated. (b) Samples annealed in O_2 at different temperatures as indicated.
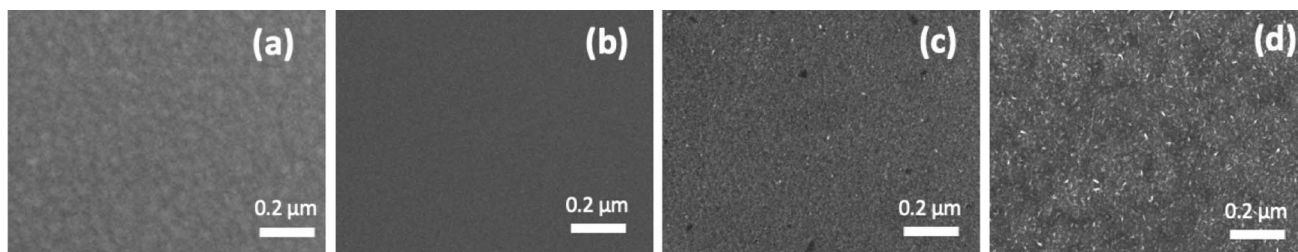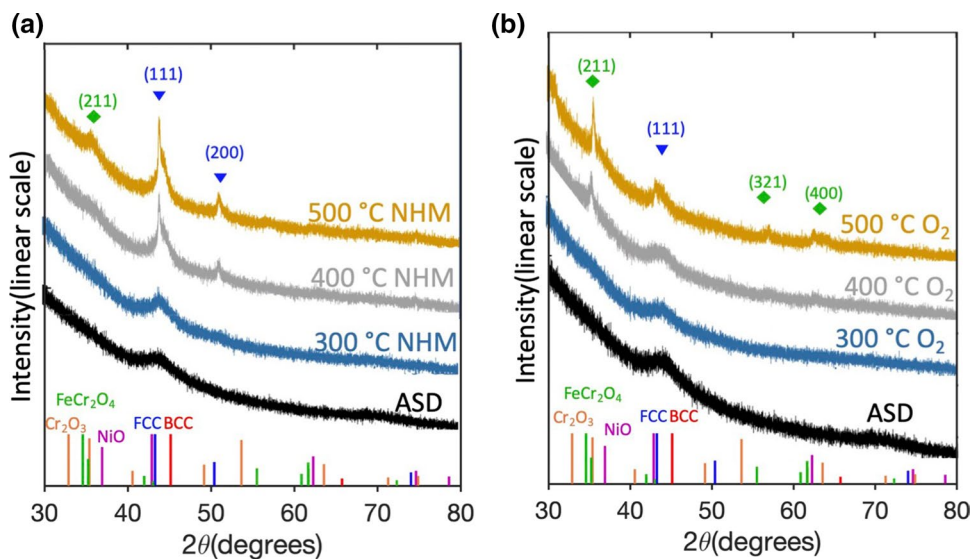

Fig. 9 SEM images of the sputtered films as deposited and annealed at different temperatures in O_2 gas for 2h. (a) As deposited (b) 300°C (c) 400°C (d) 500°.

crystalline oxides is evidenced by the XRD in Fig. 8b for the 500°C annealing. We see peaks which can be assigned to the formation of crystalline spinel structure such as $FeCr_2O_4$. We find it likely that the oxide contains Cr, while there could be a mix of other elements in it in addition to Fe. We also have a well-defined peak that can be assigned to HEA metal nanocrystals possibly with different compositions and also possibly both FCC and BCC. This is in agreement with the hypothesis of the structures and the electrical measurements if these metallic nanoparticles still form a percolating network.

Summary and Conclusions

In this work, we studied reactive sputtered films of HEA CrFeCoNiCu target by structural and electrical characterization techniques after annealing in gas ambient of, respectively, oxygen gas and nitrogen hydrogen mixture. The electrical resistivity of the films could be varied much by controlled annealing. It could be varied between 1.3×10^{-4} Ω cm and 1.2×10^{-3} Ω cm by the post-deposition processing. The temperature coefficient of resistivity could be varied between -1.2×10^{-3} K^{-1} through 0 and to $+0.7 \times 10^{-3}$ K^{-1}. The measurements and characterization were in agreement with the hypothesis that the key to the variation is controlling the topology of the film. The transport of electrons was controlled by the relative contribution of weak localization and alloy scattering by varying degree of disorder in the metallic high entropy alloy and its topology. The morphology of the film could be varied from nanocrystals of high entropy alloy to large conducting grains. The hypothesis may be applicable to a larger range of sputter parameters giving different as deposited structures, and is currently under testing.

Conflict of interest On behalf of all authors, the corresponding author states that there is no conflict of interest.

References

1. J.-W. Yeh, S.-K. Chen, S.-J. Lin, J.-Y. Gan, T.-S. Chin, T.-T. Shun, C.-H. Tsau, and S.-Y. Chang, *Adv. Eng. Mater.* 6, 299 (2004).
2. B. Cantor, I.T.H. Chang, P. Knight, and A.J.B. Vincent, *Mater. Sci. Eng. A* 375–377, 213 (2004).
3. E.P. George, D. Raabe, and R.O. Ritchie, *Nat. Rev. Mater.* 4, 515 (2019).
4. E.P. George, W.A. Curtin, and C.C. Tasan, *Acta Mater.* 188, 435 (2020).
5. C.M. Rost, E. Sachet, T. Borman, A. Moballegh, E.C. Dickey, D. Hou, J.L. Jones, S. Curtarolo, and J.P. Maria, *Nat. Commun.* 6, 8485 (2015).
6. P. Edalati, Q. Wang, H. Razavi-Khosroshahi, M. Fuji, T. Ishihara, and K. Edalati, *J. Mater. Chem. A* 8, 3814 (2020).
7. A. Sarkar, Q. Wang, A. Schiele, M.R. Chellali, S.S. Bhattacharya, D. Wang, T. Brezesinski, H. Hahn, L. Velasco, and B. Breitung, *Adv Mater* 31, e1806236 (2019).
8. S. Jiang, T. Hu, J. Gild, N. Zhou, J. Nie, M. Qin, T. Harrington, K. Vecchio, and J. Luo, *Scr. Mater.* 142, 116 (2018).
9. M. Balcerzak, K. Kawamura, R. Bobrowski, P. Rutkowski, and T. Brylewski, *J. Electron. Mater.* 48, 7105 (2019).
10. B.L. Musicó, D. Gilbert, T.Z. Ward, K. Page, E. George, J. Yan, D. Mandrus, and V. Keppens, *APL Mater.* 8, 040912 (2020).
11. H.Y. Diao, R. Feng, K.A. Dahmen, and P.K. Liaw, *Curr. Opin. Solid State Mater. Sci.* 21, 252 (2017).
12. Y. Zhang, T.T. Zuo, Z. Tang, M.C. Gao, K.A. Dahmen, P.K. Liaw, and Z.P. Lu, *Prog. Mater Sci.* 61, 1 (2014).
13. T.M. Butler, J.P. Alfano, R.L. Martens, and M.L. Weaver, *JOM* 67, 246 (2014).
14. W. Li, P. Liu, and P.K. Liaw, *Mater. Res. Lett.* 6, 199 (2018).
15. X.H. Yan, J.S. Li, W.R. Zhang, and Y. Zhang, *Mater. Chem. Phys.* 210, 12 (2018).
16. M.C. Gao, D.B. Miracle, D. Maurice, X. Yan, Y. Zhang, and J.A. Hawk, *J. Mater. Res.* 33, 3138 (2018).
17. S. Shafeie, S. Guo, P. Erhart, Q. Hu, and A. Palmqvist, *Adv. Mater.* 31, e1805392 (2019).
18. S.H. Albedwawi, A. AlJaberi, G.N. Haidemenopoulos, and K. Polychronopoulou, *Mater. Des.* 202, 109534 (2021).
19. Q. Wang, A. Sarkar, D. Wang, L. Velasco, R. Azmi, S.S. Bhattacharya, T. Bergfeldt, A. Düvel, P. Heitjans, T. Brezesinski, H. Hahn, and B. Breitung, *Energy Environ. Sci.* 12, 2433 (2019).
20. A. Sarkar, L. Velasco, D. Wang, Q. Wang, G. Talasila, L. de Biasi, C. Kubel, T. Brezesinski, S.S. Bhattacharya, H. Hahn, and B. Breitung, *Nat. Commun.* 9, 3400 (2018).
21. H. Li, Y. Zhou, Z. Liang, H. Ning, X. Fu, Z. Xu, T. Qiu, W. Xu, R. Yao, and J. Peng, *Coatings* 11, 628 (2021).
22. D. Bérardan, S. Franger, D. Dragoe, A.K. Meena, and N. Dragoe, *Phys. Status Solidi RRL* 10, 328 (2016).
23. S.R. Reddy, U. Sunkari, A. Lozinko, S. Guo, and P.P. Bhattacharjee, *J. Mater. Res.* 34, 687 (2019).
24. C. Ng, S. Guo, J. Luan, S. Shi, and C.T. Liu, *Intermetallics* 31, 165 (2012).
25. D.B. Miracle, and O.N. Senkov, *Acta Mater.* 122, 448 (2017).
26. O. Schneeweiss, M. Friák, M. Dudová, D. Holec, M. Šob, D. Kriegner, V. Holý, P. Beran, E.P. George, J. Neugebauer, and A. Dlouhý, *Phys. Rev. B* 96, 014437 (2017).
27. A. Sarkar, B. Breitung, and H. Hahn, *Scr. Mater.* 187, 43 (2020).
28. L.R. Owen, and N.G. Jones, *J. Mater. Res.* 33, 2954 (2018).

29. D. Farkas, and A. Caro, *J. Mater. Res.* 33, 3218 (2018).
30. L.R. Owen, H.J. Stone, and H.Y. Playford, *Acta Mater.* 170, 38 (2019).
31. Q. He, and Y. Yang, *Front. Mater.* 5, 42 (2018).
32. C. Li, J.C. Li, M. Zhao, and Q. Jiang, *J. Alloys Compd.* 475, 752 (2009).
33. O.N. Senkov, G.B. Wilks, D.B. Miracle, C.P. Chuang, and P.K. Liaw, *Intermetallics* 18, 1758 (2010).
34. Y.F. Ye, Q. Wang, J. Lu, C.T. Liu, and Y. Yang, *Mater. Today* 19, 349 (2016).
35. D. Ma, B. Grabowski, F. Körmann, J. Neugebauer, and D. Raabe, *Acta Mater.* 100, 90 (2015).
36. A. Aliyu, M.Y. Rekha, and C. Srivastava, *Philos. Mag.* 99, 718 (2018).
37. D. Gaertner, J. Kottke, G. Wilde, S.V. Divinski, and Y. Chumlyakov, *J. Mater. Res.* 33, 3184 (2018).
38. M.Y. Rekha, N. Mallik, and C. Srivastava, *Sci. Rep.* 8, 8737 (2018).
39. R. Wang, W. Chen, J. Zhong, and L. Zhang, *J. Mater. Sci. Technol.* 34, 1791 (2018).
40. L.R. Shaginyan, V.F. Britun, N.A. Krapivka, S.A. Firstov, A.V. Kotko, and V.F. Gorban, *Powder Metall. Met. Ceram.* 57, 293 (2018).
41. A. Mao, H. Xiang, X. Ran, Y. Li, X. Jin, H. Yu, and X. Gu, *J. Alloys Compd.* 775, 1177 (2019).
42. A. Verma, P. Tarate, A.C. Abhyankar, M.R. Mohape, D.S. Gowtam, V.P. Deshmukh, and T. Shanmugasundaram, *Scr. Mater.* 161, 28 (2019).
43. R. Dedoncker, G. Radnóczi, G. Abadias, and D. Depla, *Surf. Coat. Technol.* 378, 124362–124371 (2019).
44. J. Mayandi, M. Stange, E. Sagvolden, M.F. Sunding, M. Schrade, J. Deuermeier, E. Fortunato, O.M. Løvvik, A. G. Ulyashin, S. Diplas, P. Carvalho, and T.G. Finstad, https://arxiv.org/abs/2108.08373 [cond-mat.mtrl-sci].
45. N.F. Mott, *Metal Insulator Transitions* (London: Taylor and Francis, 1974).
46. A.L. Efros, and B.I. Shklovskii, *J. Phys. C: Solid State Phys.* 8, L49 (1975).
47. P. Stallinga, *Adv Mater* 23, 3356 (2011).
48. J. Mayandi, T. G. Finstad, Ø. Dahl, P. Vajeeston, M. Schrade, O.M. Løvvik, S. Diplas, and P. Carvalho, *Thin Solid Films*, Submitted (2021).
49. K. Jin, B.C. Sales, G.M. Stocks, G.D. Samolyuk, M. Daene, W.J. Weber, Y. Zhang, and H. Bei, *Sci Rep* 6, 20159 (2016).
50. J. Kondo, and A. Hewson, *Scholarpedia* 4, 7529 (2009).
51. M. Chand, A. Mishra, Y.M. Xiong, A. Kamlapure, S.P. Chockalingam, J. Jesudasan, V. Bagwe, M. Mondal, P.W. Adams, V. Tripathi, and P. Raychaudhuri, *Phys. Rev. B* 80, 134514 (2009).
52. B. Sundqvist, and V.K. Tolpygo, *J. Phys. Chem. Solids* 122, 41 (2018).
53. Y. Werman, and E. Berg, *Phys. Rev. B* 93, 075109 (2016).
54. Z. Fisk, and G.W. Webb, *Phys. Rev. Lett.* 36, 1084 (1976).
55. W.H. Butler, *Phys Rev B Condens Matter* 31, 3260 (1985).
56. J.H. Mooij, *Phys. Stat. Sol. (A)* 17, 521 (1973).